A mm-Wave Switched-Capacitor RFDAC

Hieu Minh Nguyen, *Graduate Student Member, IEEE*, Jeffrey Sean Walling, *Senior Member, IEEE*,
Anding Zhu, *Fellow, IEEE*, and Robert Bogdan Staszewski, *Fellow, IEEE*

Abstract—This article proposes an interleaving switched-capacitor RF digital-to-analog converter (RFDAC) using an edge combiner within the output stage to implicitly triple its effective clock carrier frequency and enable the mm-wave (mmW) operation. Tripling in the output stage allows for increased energy efficiency, which is further improved by employing an edge-combining-based frequency-tripling delay-locked loop (DLL) in the clock generation network. The clock tripling is performed in each slice of the switched-capacitor PA (SCPA), which allows yet another 3× frequency reduction for the global clock distribution. Finally, a new layout structure accounts for transmission-line (TL) effects, due to the large physical size of the passive capacitor array. Implemented in 22-nm FD-SOI, the prototype achieves $P_{out} > 21$ dBm, drain efficiency $>36\%$, and system efficiency $>22\%$ while operating in the *Ka*-band at 28 GHz. Modulation at 2.4 Gb/s results in 3.3% EVM and 30.8-dBc adjacent channel leakage ratio (ACLR).

Index Terms—Class D, clock distribution, digital PA (DPA), edged combining (EC), mm-wave (mmW), power combining, RF digital-to-analog converter (RF-DAC), switched-capacitor power amplifier (SCPA), transmitter (TX).

I. INTRODUCTION

SINCE the introduction of "digital RF" [1], digital transmitters (TXs) have gained a lot of interest due to their amenability to CMOS technology scaling. Many digitally intensive TX designs have followed over the years with ever improving performance [2]–[7]. Their subset, digital power amplifiers (DPAs) and RF digital-to-analog converters (RFDACs), have consistently become more competitive when compared to traditional analog PAs, particularly in the sub-6-GHz range. With modern 5G signals, the demand for higher output power, higher energy efficiency (at peak and back-off output power), and increased linearity are the key

Fig. 1. Issues when attempting to design a conventional digitally intensive *I/Q* RFDAC architecture in mmW.

considerations. In addition, the ability to operate at mm-wave (mmW) is gaining importance.

DPAs and RFDACs combine the functionality of a DAC+mixer and power combiner, as shown in Fig. 1. They are amenable to technology scaling due to utilizing the transistor as a switch. In general, they can be classified into two architectures based on their signal summation (e.g., current and voltage modes). For the current-mode architectures, several innovative designs have been presented. In [4], the current-mode-based class-E switching PA utilized single-MOS devices as power switches for the RFDAC's unit cell, which is easy to implement but requires digital pre-distortion (DPD) to achieve linear operation. In addition, a power-combining network was required to obtain high output power, and the power supply was increased, resulting in potential reliability issues. In contrast, voltage-mode structures [e.g., switched-capacitor PA (SCPA)] [2], [5], [8], [9] show better reliability (due to fixed voltage swings on all devices) and linearity without using DPD. In fact, the SCPA can exhibit improved linearity compared to analog PAs [10] without compressive behavior when bondwires are properly accounted for. Hence, the SCPA typically does not require additional output power backoff for linear operation [11]. In addition, RFDACs[1] typically offer improved energy efficiency when compared to analog PAs. At sub-6-GHz frequencies, RFDAC structures have been recently improved with many innovations that focus on increasing the back-off efficiency using switched transformers [12]–[14] or sub-harmonic LO techniques [15], [16]. A key challenge with RFDACs is that they have mostly been limited in operational frequency due to the

---

[1]The terms DPA and RFDAC are used interchangeably in the literature, although the latter might indicate a higher resolution and/or (historically) lower output power.

limited ability for a transistor to switch at higher frequencies. In contrast, analog PAs can operate at any frequency up to the transistor's f_{max}. Because of this, CMOS analog PAs are dominant at mmW frequencies, with many architectures proposed to obtain improved performance in key metrics of linearity, output power, and efficiency.

Recently, a current-mode inverse-outphasing TX [17] and a Doherty PA [18] were introduced to work in the Ka-band and obtained high efficiency (>30%) with high output power (>20 dBm). Outphasing and Doherty architectures have proven reliable in improving back-off efficiency. However, they require a complex passive output network to implement that may limit usable bandwidth. To operate as digital TXs, the aforementioned architectures also require a high-speed DAC that decreases the system efficiency, η_{SE} [18]. To overcome this, power DACs [19], [20] have shown promise. In [19], multi-stacked power MOSFETs were proposed to work as DACs at mmW, while Gilbert cells were used as up-converters; however, due to the wide-bandwidth specification, the peak η_{SE} was reduced to 10.3%. In addition, at mmW, distributed effects contribute significantly to load-impedance variation, resulting in output power reduction. The synthesized impedance variation technique shows a means to compensate for the distributed effects in the combination network and increases η_{SE} up to 22%. A DPA with non-constant envelope-modulation class-E at 60 GHz in [21] obtained 17.7% efficiency, while a polar RFDAC with a transformer-coupled two-stage PA [22] achieved 15.3% efficiency.

Through all of the efforts to bring RFDACs to the mmW band, the biggest issue is the reduction of efficiency in the output stage, thus ruining the total system efficiency and wideband operation. First, deploying *polar* RFDACs is not advisable due to the polar bandwidth expansion [1]; hence, *I/Q* architectures are the best choice for mmW wide-bandwidth requirements. The efficiency degradation at mmW comes from three primary sources. As shown in Fig. 1, the conventional *I/Q* RFDAC [3] contains a logic gate that is implemented to mix the LO signal with the baseband data ①. Due to the high frequency of operation, generating the LO to switch the output stage is challenging and consumes significant power, causing the degradation of η_{SE} ②. This signal then controls a parallel bank of switches/current sources that are summed/combined at the output before being fed to the antenna ③. In this case, the node where the switches/current sources are combined must account for the distributed effects at mmW. Beyond this, the switching elements are constructed from MOS devices with limited switching speed due to the parasitic device capacitance. As a result, hard switching is not generally possible at mmW [23]. In addition to efficiency, achieving good linearity has proven difficult for mmW RFDACs because to date all have operated in the current domain. Current division causes saturation of the output voltage characteristic in this domain; hence, it has been necessary to use low-to-moderate bandwidth signals with complicated DPD to meet linearity requirements.

To solve the challenges limiting RFDACs at mmW, an edge-combining (EC) SCPA (EC-SCPA) is presented for the first time. The EC-SCPA uses an embedded frequency multiplier to bring the voltage-mode RFDAC to Ka-band operation,
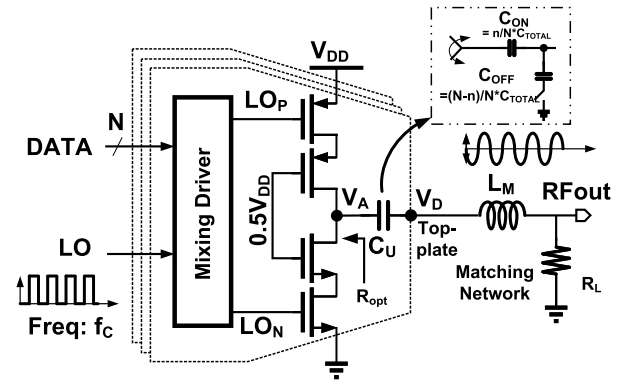
Fig. 2. Conventional SCPA architecture.

maintaining similar linearity and efficiency associated with lower frequency SCPAs. In the proposed EC-SCPA, the system efficiency is enhanced by embedding sub-harmonic injection-locking techniques to generate the LO/clock signals, and a novel partitioned layout allows for overcoming distributed layout effects. The proposed EC-SCPA achieves peak drain efficiency $\eta = 36\%$ and system efficiency $\eta_{SE} = 22\%$ with good linearity while transmitting single-carrier 16- and 64-QAM signals.

This article is organized as follows. Section II explains the limitations and main challenges in bringing RFDACs to mmW based on SCPA analysis and investigation and then shows the proposed circuit innovation architecture for the mmW RFDAC. Section III describes the circuit implementation. Measurement results and discussion are presented in Section IV, which showcases the performance of the prototype design.

II. PRESENT LIMITATIONS AND PROPOSED SOLUTIONS

A. Conventional SCPA at mmW

Voltage-mode RFDACs (e.g., SCPAs [2]) have proven nearly optimal for wireless TXs in CMOS because they occupy a small chip area, are energy efficient, and benefit from technology scaling. Every transistor in an SCPA is switched ON/OFF at the carrier frequency rate of f_c (i.e., the devices are not linear current sources); hence, the power consumption scales with $CV_{DD}^2 f_c$. The SCPA is a segmented class-D amplifier (see Fig. 2) where switches and capacitors are segmented into parallel paths that are digitally enabled (disabled) to increase (decrease) the RF output voltage, thereby providing an overall linear amplitude control at the RF output. The cascoded switch requires two voltage supplies V_{DD} and $0.5 \times V_{DD}$, but it is noted that a cascode is not required, particularly for low-power operation. The total capacitance seen from the inductor is the sum of all unit capacitors C_{unit}. In ideal operation, the inductor L_M is resonant with the sum of all capacitors, and the resistor is equal to the optimal termination resistance, R_{opt}. L_M and R_{opt} can be replaced with an output-matching network, transforming from a fixed output impedance (e.g., 50 Ω) to the presented equivalent.

The RFDACs have proven competitive for sub-6-GHz cellular and connectivity applications [4], [24]–[27]. They combine

the embedded DAC and mixer functionalities with high RF output power capability into a single, energy-efficient, and globally linear block that utilizes only switching transistors. In the development and deployment of 5G technology, the mmW band plays a vital role. Hence, significant work has been done in mmW transceivers. Bringing direct-digital transmitters, including RFDACs [21], [22], to the mmW band has proven challenging due to the limited switching speed of CMOS transistors. Although challenging to implement, there are obvious advantages to the direct-digital RFDAC approach, such as enabling fully connected digital beamforming [9].

To understand the challenges in pushing RFDACs into the mmW territory, we first assume a traditional RFDAC designed as represented by the SCPA in Fig. 2. It receives the N-bit digital baseband input signal DATA$\langle N{:}1\rangle$, which is then mixed with the carrier clock of frequency f_c by a logic gate residing in each individual RFDAC cell. The outputs of the RFDAC cells are combined and filtered by the LC tank to generate the modulated output RF$_{\text{out}}$. The RFDAC is a combination of the switched unit cells; hence, the switching speed of the RFDAC is limited by the transition frequency, f_T, of the MOS devices that are utilized as switches. However, this is dependent on the process technology. Hence, the highest operational frequency of the RFDAC, while maintaining the aforementioned advantages, is an initial point of investigation.

Now, a brief review of the SCPA follows. The SCPA is effectively an SC RFDAC. The unit cells of the SCPA are switched at the RF carrier frequency, f_c, between V_{DD} and V_{GND} or held at V_{GND} based on the input control signal that is derived from the input digital baseband being a binary N-bit stream operating at the rate of f_{BB}, which is typically $\ll f_c$. For a certain input code, a proportional capacitance (C_{ON}) will be undergoing the switching, while the disabled capacitance (C_{OFF}) is shorted to the ground. The total capacitance is $C_{\text{total}} = C_{\text{ON}} + C_{\text{OFF}}$. The top-plate voltage V_D amplitude produced by the capacitor array can be calculated by scaling the supply voltage by the ratio of the enabled capacitance to the total capacitance: $V_D = (C_{\text{ON}}/C_{\text{total}}) \times V_{\text{DD}}$. V_D is converted to RF$_{\text{out}}$ using a matching network that is resonant at the same frequency as the switching rate f_c. In theory, the ideal total efficiency (η) is 100% when considering lossless switches and passives. In practice, based on the conventional derivation from [2], the total system efficiency η_{SE} can be defined as the following equation, which only accounts for the switches and drivers

$$\eta_{\text{SE}} = \frac{P_{\text{out}}}{P_{\text{dc}}} = \frac{P_{\text{out}}}{P_{\text{out}} + P_{\text{loss}} + P_{\text{driver}}} \tag{1}$$

where P_{out} is the RF output power, the driver burns P_{driver}, and P_{loss} represents the combination of the switching P_{sw} and dynamic P_{SC} losses, which are calculated as follows:

$$P_{\text{SC}} = \frac{(N-n)N}{N^2} C_{\text{total}} V_{\text{DD}}^2 f_c \tag{2}$$

$$P_{\text{sw}} = \frac{n}{N} C_{\text{sw}} V_{\text{DD}}^2 f_c \tag{3}$$

where $n(N-n)$ is the number of active unit cells that are turned on (off) at the RF carrier rate f_c. The two losses in (2) and (3) depend on f_c. At sub-6 GHz, the unit capacitor
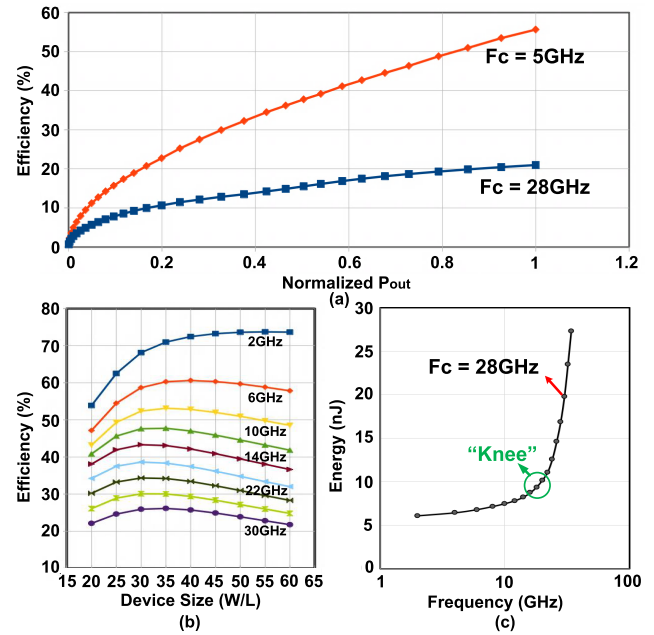
Fig. 3. Simulated drain efficiency (η) plots of the conventional SCPA: (a) versus normalized P_{out} at 5 and 28 GHz and (b) versus device size W (L stays minimum) at different frequencies of operation. (c) Energy per cycle versus frequency.

$C_u = C_{\text{total}}/2^N$ is significantly larger than the switch parasitic capacitance and the parasitic components of the impedance-matching network. Hence, the dynamic power loss from the switch array has a lower effect on η. At mmW, the physical size of the passive impedance-matching network is reduced. Furthermore, the increased frequency is accompanied by a reduction of the total capacitance required in the capacitor array such that its C_u is comparable to the parasitic capacitance of the switches. Hence, the parasitic capacitors (e.g., C_{gs} and C_{ds}) have a significant impact on reducing η. To quantify the impact, the parasitic capacitors are added into (2) as C_{par}, which is rewritten as follows:

$$P_{\text{SC}} = \frac{(N-n)N}{N^2}\left(C_{\text{total}} + C_{\text{par}}\right)V_{\text{DD}}^2 f_c. \tag{4}$$

Therefore, P_{total} is reduced by the factor $C_{\text{par}}V_{\text{DD}}^2 f$. In addition, at mmW, the switching frequency f_c will degrade the output power P_{out} because the switching pulses will have relatively slower transitions due to the f_T limitations of the switching devices.

To offer a better intuition of how increasing f_c impacts the design, a 6-bit model is created in which the normalized output power is constrained to be constant across f_c. The "experiment" uses real MOS device models from the commercial 22-nm FD-SOI PDK. Two cases are tested: at 5 and 28 GHz at the same $P_{\text{out}} = 19$-dBm target. The resulting plots of η versus P_{out} are shown in Fig. 3(a). At $f_c = 5$ GHz, η obtained from the model is almost 60% but reduces to 20% at $f_c = 28$ GHz. With this, the system efficiency η_{SE}, which includes all the required power to operate the SCPA, will further degrade significantly. This level of η_{SE} makes the standard SCPA not competitive at mmW even when compared to linear amplifiers (e.g., class-B).
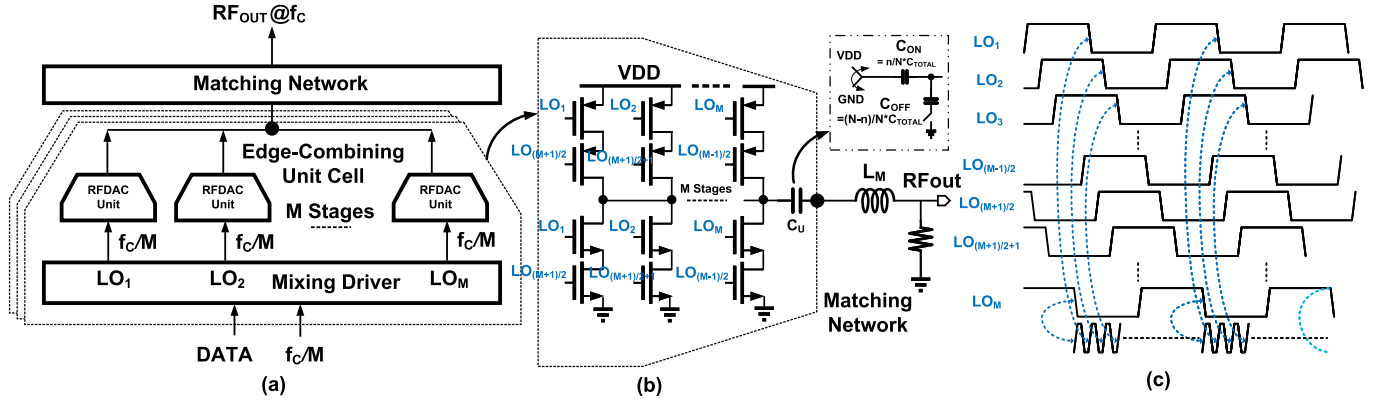
Fig. 4.   Proposed idea of three-slice edge-combining SCPA: (a) block diagram and (b) circuit schematic of the single slice. (c) Timing diagram illustrating the edge-combining frequency multiplication. (Note: in this labeling scheme, M is restricted to odd numbers.)

Next, the driver power is also considered. It can be calculated as

$$P_{\text{driver}} = \frac{n}{N} C_{\text{driver}} V_{\text{DD}}^2 f_c \qquad (5)$$

where C_{driver} is the total capacitance along the driver chain. Because the driver is associated with the switching inputs, its power drain is added to the denominator in (1), thereby reducing η_{SE}. It is thus clear that operating the standard SCPA at mmW would burn huge power in the driver. It is further noted that the switching might actually be nearly impossible at mmW due to the limited f_T of the devices, meaning that the expected "square-wave" operation would not be possible [23].

As with any TX that includes an RF PA, the design of RFDACs involves tradeoffs between the efficiency (e.g., η and η_{SE}), output power (P_{out}), and dimensions of the output stage power device (e.g., W/L). To a first order, P_{out} is proportional to W/L. However, a larger W does not necessarily lead to increased efficiency, due to the previously discussed parasitic effects. Using our model, we sweep W for carrier frequencies ranging 2–34 GHz. The resulting efficiency is plotted in Fig. 3(b). As predicted, the efficiency decreases as the frequency increases. Also of note is that the efficiency generally peaks for smaller device sizes. This makes sense, as the parasitic power is increased with W. However, although the efficiency may have an optimal value for a smaller W, this will also keep a limit on P_{out}. This tradeoff is exacerbated at higher frequencies, where maintaining the specified power requires increasing the device size and operating farther from the optimal size for peak efficiency.

Another interesting comparison is the energy usage per cycle, $E_{\text{dc}} = \int_0^{1/f_c} P_{\text{dc}}(t) dt$, as a function of f_c. Here, the model is scaled to keep the same $P_{\text{out}} = 19$ dBm. The results are plotted in Fig. 3(c) and clearly show that significantly more energy is spent at higher frequencies to deliver the same P_{out}.

Hence, two problems associated with mmW operation of the SCPA can clearly be identified (provided, of course, that the technology is fast enough to ensure the reliable switching of devices) as follows.

Problem II-1: The efficiency is reduced due to the increase in dynamic power consumption, due to the parasitic resistance
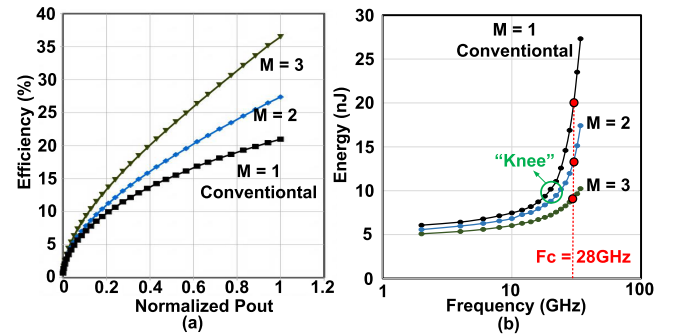
Fig. 5.   Simulated energy plots for the conventional ($M = 1$) and frequency multiplying ($M = 3$) SCPA: (a) efficiency versus normalized P_{out} at 28 GHz and (b) energy per cycle versus frequency. Note: at each frequency point, the circuit is re-optimized and re-simulated.

and capacitance. This is exacerbated when the unit capacitance is comparable to the switch parasitic capacitance.

Problem II-2: More power is consumed by drive switches at mmW, resulting in significant η_{SE} degradation.

B. Proposed Edge Combiner Based on XOR Function Switches

First, considering (2) and (3), P_{SC} is difficult to reduce due to its intrinsic dependence on C_{total}, which is tied to the resonant network construction. However, reducing the dynamic losses of the switches and the driver appears more feasible. *Prima facie,* reducing the switching frequency of the MOS switching devices appears to reduce the power consumption linearly, proportional to the reduction in switching rate. However, irrespective of the final recombination technique used (e.g., edge combiner, parallelism/interleaving, and pipelining), the net rate of effective edges in the switched-mode PA architecture (such as our SCPA) cannot change as it must be the same as the carrier frequency, f_c. Consequently, P_{sw} would stay the same, assuming that C_{sw} is invariant. For this reason, it is more intuitive to consider the consumed energy per cycle rather than the power: $E_{\text{SC}} = P_{\text{SC}} f_c = n/N C_{\text{sw}} V_{\text{DD}}^2$. A quick glance at Fig. 5(c) reveals that E_{SC} (thus, C_{sw}) stays relatively constant at lower frequencies but then suddenly

starts fiercely increasing in an exponential-like manner. This region of sudden expansion is termed "knee." Operating below the knee ($\sim$10 GHz) would ensure the optimally low energy consumption. However, the final switch rate of $\sim$30 GHz will be regained using the proposed edge-combining (EC) frequency multiplication technique that acts as an interleaver.

The proposed interleaving SCPA architecture is shown in Fig. 4(a). The input LO frequency f_{LO} is reduced from f_c to f_c/M, where M is the implicit clock multiplication factor via the proposed edge combining of 1-bit up-converted data. Each SCPA unit cell now switches at f_c/M, which is M times lower than in the conventional architecture, which means likely operating below the energy knee.

A multiply-by-M SCPA stage is shown in Fig. 4(b). The circuit leverages the same mechanism that allows a digital XOR gate to obtain frequency multiplication. In the two-input XOR gate, if the inputs are at the same frequency, but offset in phase, the output will be at $2\times$ the input frequency. Additional branches can be added, which enables higher multiplication factors. The output-matching network can be tuned to be resonant at f_c. In the multiplying circuit, there are now $M\times$ as many branches as in the conventional SCPA. To a first order, there are now M switching elements, operating at f_c/M; hence, the power consumption should be the same, but the switches now operate below the energy knee of Fig. 3(c). Thus, they can be substantially reduced in size. P_{sw} is now re-defined as

$$P_{sw} = \frac{n}{N}\left(MC'_{sw}\right)V_{DD}^2\left(\frac{f_c}{M}\right) \tag{6}$$

where C'_{sw} represents the parasitic capacitance of the modified (smaller) switch for the reduced switching frequency from f_c to f_c/M.

A model of the interleaving SCPA is constructed for comparison with the conventional SCPA. It is simulated for three different frequency multiplication factors $M = 1, 2, 3$, to produce 28 GHz. The simulated efficiency as a function of the normalized output power is plotted in Fig. 5(a). The peak efficiency for the case of $M = 2$ increases by 8% compared to the conventional ($M = 1$) case, while for $M = 3$, it increased by $\sim$18%. The energy per carrier cycle for the three cases is plotted in Fig. 5(b) and shows great improvement, especially at mmW frequencies.

As noted above, higher values of M are possible with more parallel branches and could lead to further reduction in the power consumption of the output stage at higher carrier frequencies, i.e., beyond the "knee" of Fig. 5(b) where the interleaving overhead cost happens to be lower than the potential energy savings. To operate with $M > 3$, more phases are required, so the edge combiner (later shown in Fig. 10) would need to be re-designed. This would lead to an additional overhead in energy consumption for the generation and distribution of the phases, which reverses some of the power reduction in the output stage.

The benefits of the SCPA interleaving extend also to the drivers as they individually switch at the likewise lower frequency, f_c/M, allowing to reduce their size. Equation (6)
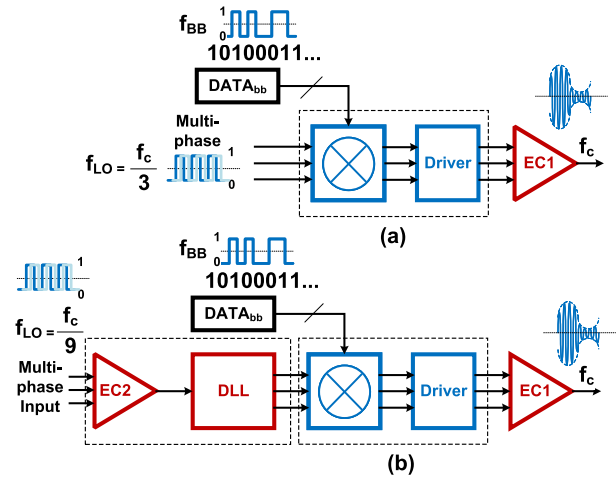
Fig. 6. EC frequency multiplication: (a) only at the output stage and (b) at both the output stage and the clock generation.

can be extended in a similar manner to the driver network

$$P_{driver} = \frac{n}{N}\left(MC'_{driver}\right)V_{DD}^2\left(\frac{f_c}{M}\right) \tag{7}$$

where C'_{driver} is the total capacitance in the single driver chain. Due to the operation at lower frequency, the driver chain's transistor width can now be optimally sized for both energy usage and edge rate. This allows for more efficient operation. This was explained above in conjunction with operating below the energy knee of Fig. 5(b).

C. Proposed Edge-Combining SCPA Architecture

In a step to realize the aforementioned advantage of frequency multiplication via interleaving within the output stage of the mmW SCPA, we can draw the resulting architecture in Fig. 6(a). A three-way edge combiner (EC1) is used to *implicitly* multiply the input frequency $3\times$. Hence, the input LO frequency is $f_c/3$. The digital baseband data are mixed logically with the carrier sub-harmonic to generate the modulated signal before passing through the buffer stage in order to drive the edge-combining switch-cap unit cell EC1.

It is noted that in the case of an output frequency of $f_c \approx 27$ GHz, the distribution of the input clock waveform $f_{LO} \approx 9$ GHz can still be cumbersome. Hence, a further power reduction is made to apply the edge combining to the clock generation and distribution. This is shown in Fig. 6(b). The input f_{LO} frequency multiplication by $3\times$ uses and edge combiner EC1 followed by a delay-locked loop (DLL). The details will be provided in the following. In this scenario (and still maintaining $M = 3$), the clock power consumption is given as follows:

$$P_{LO} = 9\,C_{clk}V_{DD}^2\left(\frac{f_c}{9}\right) \tag{8}$$

where C_{clk} is the total capacitance in the single clock distribution chain. Just as in the previous cases, here by allowing to operate at $\sim$3 GHz in each chain, the device sizes can be reduced for the overall net reduction in the entire C_{clk}.
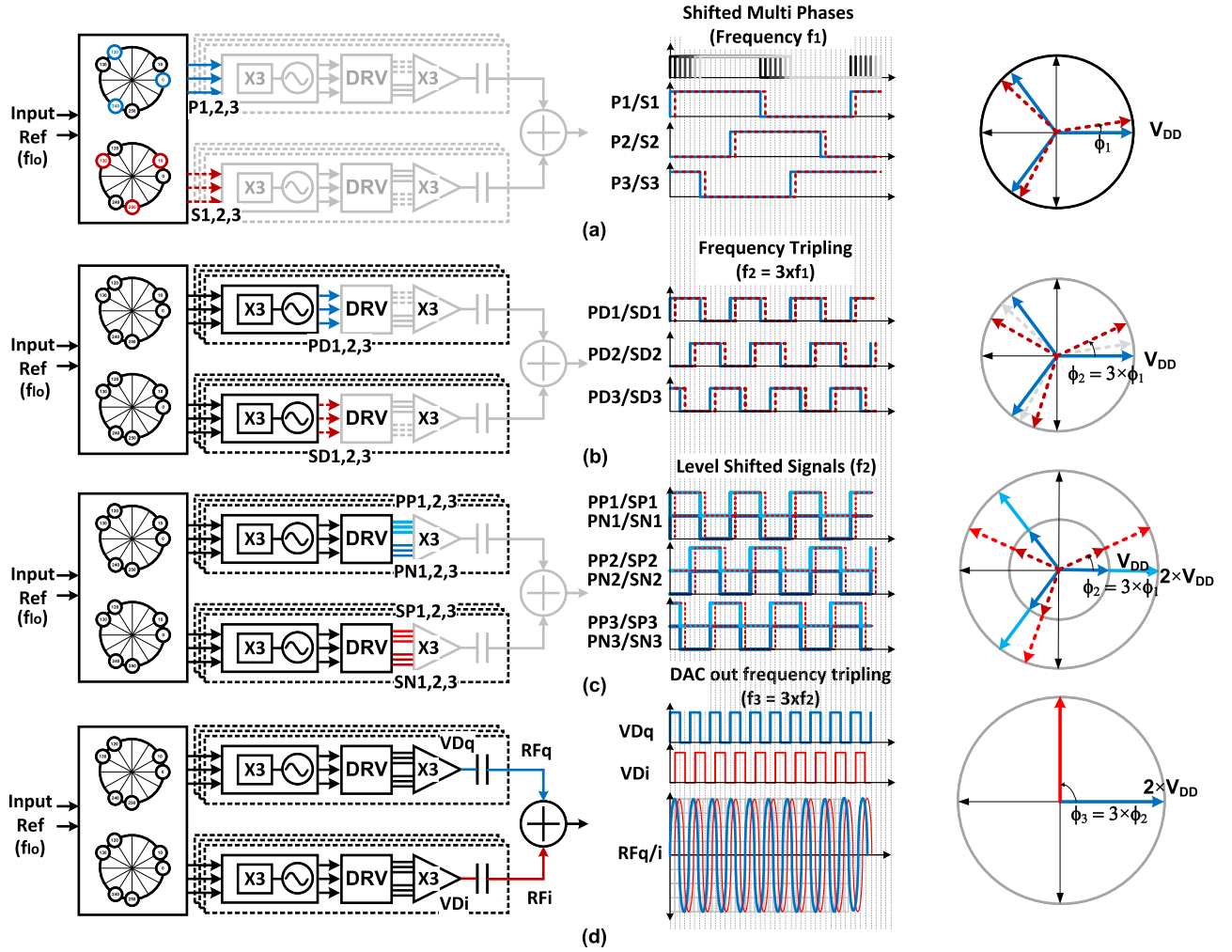
Fig. 7. Conceptual development steps in diagrams and waveforms leading to the proposed SCPA. (a) Multi-phase signals generated at f_1. (b) Frequency tripling to $f_2 = 3 \times f_1$ by the edge-combining local DLL. (c) Multi-phase signals buffed and level-shifted. (d) Edge-combining frequency tripling at the output stage.

To accomplish a complex modulation, one EC-SCPA is dedicated to the in-phase (I) data path, while another to the quadrature (Q) path. The power combiner at the end merges their two outputs. The operational block diagram is presented in Fig. 7. The global injection-locked oscillator generates multi-phase signals at f_1 frequency: $P_{1,2,3}$ for the I path and $S_{1,2,3}$ for the Q path, as shown in Fig. 7(a). The phase separation between the corresponding S and P signals is ϕ_1 (90°/9 = 10°, in this case). The three phases, P_1 (S_1), P_2 (S_2), and P_3 (S_3), are each shifted 120° relative to one another. Each SCPA slice has a local DLL, into which P and S are directly injected to generate the tri-phase signals $PD_{1,2,3}$ and $SD_{1,2,3}$, as shown in Fig. 7(b). Due to the frequency multiplication, the phase is advanced by the multiplication factor 3×. All output swings are between the full rail-to-rail levels of 0 and V_{DD}. Signals PD and SD serve as the input of the logical mixer to up-convert the baseband data and to drive the EC-SCPA unit cell [see Fig. 7(c)]. Because the proposed XOR frequency-tripler circuit requires dual-level input for pMOS and nMOS, high-speed level shifters are designed to bring the three-phase signal swing from 0–V_{DD} to V_{DD}–2×V_{DD} [see Fig. 7(c)] to drive the pMOS switches.

To obtain the aligned phases for both pMOS and nMOS switches, buffer chains are added to the nMOS driver to correct any delay mismatch. After mixing with the data, the dual-level three-phase signals drive the EC switches and triple the f_2 signal to $f_3 = 3 \times f_2$ carrier frequency [see Fig. 7(d)]. The details of the system implementation are presented next.

III. CIRCUIT IMPLEMENTATION

The top-level full-chip block diagram of the proposed Ka-band switched-capacitor RFDAC is shown in Fig. 8. The digital baseband I/Q data are generated off-chip by a digital pattern generator in an FPGA and input to the IC chip via high-speed LVDS buffers. The RFDAC is designed with 2×6 bit resolution to support modulation of up to 64-QAM. The resolution choice of 6 bit was driven by the SNR requirements to achieve the 64-QAM modulation while minimizing the capacitor array size. To maximize the RFDAC linearity, it is realized as a fully unary-weighted converter, which helps to minimize both AM-AM and AM-PM distortions. The data are input to the chip in the binary format; hence, a 6-to-63 binary-to-thermometer encoder can control the individual RFDAC slices. Each slice is enabled/disabled via a
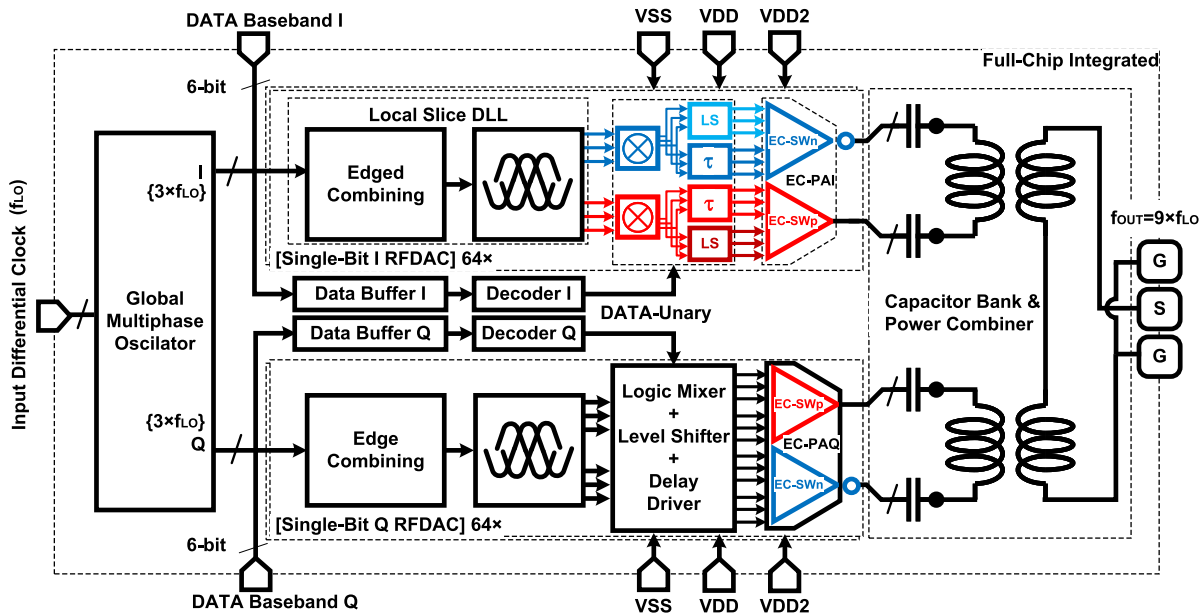
Fig. 8.   Block diagram of the full-chip implementation of the proposed mmW SC RFDAC.

logical AND with the local DLL-generated clock; hence the AND gate serves as a mixer of the data with the subharmonic-carrier clock, thus performing the first-stage up-conversion of the baseband data. Subsequently, a vector of these ON–OFF modulated clock waveforms is buffered to be strong enough to drive the output stage.

The chip receives a differential reference clock at $f_1 = f_{\text{LO}} = 2.5$–3.5 GHz, which is ultimately multiplied by 9 to reach the mmW carrier frequency range. The reference is injected to the global oscillator, which is a six-stage differential ring oscillator (RO); hence, it has 12 unique output phases. These 12 phases are required so that the correct phases are available for quadrature operation after the frequency multiplication. The proper output phases are selected and fed to the local in-slice DLLs. The edge combing at the input of the DLL network increases the injecting clock signal frequency to $f_2 = 3 \times f_{\text{LO}}$. The output of each local in-slice DLL is fed to the corresponding RFDAC bit-slice unit cell, which contains the logic mixer, the driver, and the EC output stage tripler to bring the frequency from f_2 to $f_3 = 9 \times f_{\text{LO}}$ at the RFDAC output pad (see Fig. 8). The capacitor bank is embedded in the impedance-matching network and the on-chip power-combining transformer (PCT) merges the individual I/Q signal branches. The PCT is chosen to be a parallel–parallel topology, which reduces imbalance in the structure and aids in increasing the isolation between the input channels [28], [29]. The details of the individual blocks are discussed next.

A. Output-Matching Network

It consists of the PCT and the capacitor array to provide impedance transformation from the fixed $Z_{\text{load}} = 50\text{-}\Omega$ output load to match the optimal termination impedance Z_{opt} of the output stage switches. First, the EC-SCPA is optimized for the case of maximum output power, $P_{\text{out,max}}$, when all unit cells
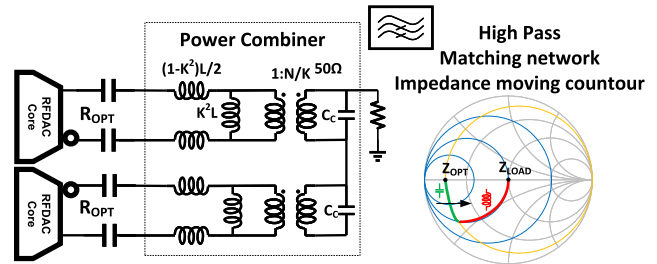
Fig. 9.   Equivalent schematic of the transformer-based output-matching network.

are ON. The optimal resistance is defined as [2]

$$R_{\text{opt}} = \frac{2}{\pi^2} \times \frac{V_{\text{DD}}^2}{P_{\text{out,max}}}. \tag{9}$$

Using the value found in (9) and assuming that the network is approximately series-resonant, the loaded quality factor of the network, Q_{load}, can be calculated as follows:

$$Q_{\text{load}} = \sqrt{\frac{Z_{\text{load}}}{R_{\text{opt}}} - 1} = \frac{1}{2\pi f_{\text{out}} C_{\text{total}} R_{\text{opt}}} \tag{10}$$

where C_{total} represents the total array capacitance of the EC-SCPA. In the presented design, $Z_{\text{opt}} = 4\ \Omega$; hence, Q_{load} is approximately 3.4 and C_{total} is approximately 437 fF. From this, the equivalent series inductance L to resonate-out the array capacitance can be found as

$$L = \frac{Q_{\text{load}} Z_{\text{opt}}}{2\pi f_{\text{out}}}. \tag{11}$$

This inductance can be embedded in the transformer, as shown in the schematic of Fig. 9. The matching network is a bandpass filter that converts Z_{opt} to Z_{load}, as illustrated in the accompanying Smith chart. Note that Q_{load} is limited by the quality
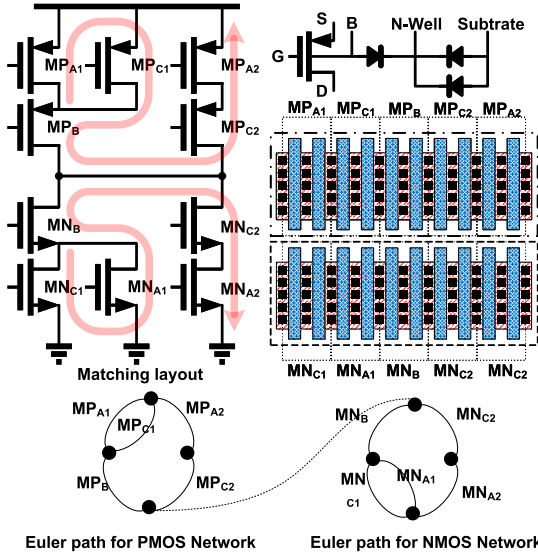
Fig. 10. XOR-based frequency-tripling edge combiner switch using deep n-well SVLT devices and the corresponding layout. (Bottom) Abstract Euler path diagram for the pMOS and nMOS networks.

factor of the on-chip PCT, Q_{xfmr}, which varies from 11 to 18. To find the optimal capacitance for maximum efficiency, the switch size can also be embedded in the optimization procedure, which was highlighted in [30].

B. Edge-Combining Frequency-Tripling XOR *Gate*

The schematic of the proposed frequency-tripling XOR-based edge combiner is shown in Fig. 10. Compared to the conventional SCPA switching circuit where there are only two phases required for the operation (e.g., ON/OFF), the tripling circuit requires three phases, as shown in Fig. 7(c). To reduce the switching losses, the closing of the pMOS switches should be in phase with the opening of the nMOS switches and vice versa. The layout parasitic capacitance should be minimized to reduce its effect on the phase mismatch; otherwise, it will increase dynamic power losses due to a so-called "crow-bar" current. In the EC tripler, the switching frequency of each individual transistor is $f_{\text{out}}/3$. Although it is easier to meet the specifications at the reduced switching speed, the proper choice of devices is still important. In this design, the transistor devices of super-low threshold voltage in deep n-well ("SLVT-deep-NW") are used for the device isolation and the ability to control the back-gate bias. Control of the back-gate bias allows to increase the switching speed by further reducing the threshold voltage of the SLVT devices.

Because there are three potential closure paths for both the pull-up and pull-down branches, precise phase accuracy is required to ensure the minimal crow-bar current. The function of the tripling XOR-gate is given as

$$F = \Phi_A \oplus \Phi_B \oplus \Phi_C. \tag{12}$$

This function can be rewritten as follows:

$$F = \left(\overline{\Phi_A}\Phi_B + \Phi_A\overline{\Phi_B}\right) \oplus \Phi_C$$
$$= \left(\overline{\Phi_A}\Phi_B + \Phi_A\overline{\Phi_B}\right)\overline{\Phi_C} + \overline{\left(\overline{\Phi_A}\Phi_B + \Phi_A\overline{\Phi_B}\right)}\Phi_C. \tag{13}$$
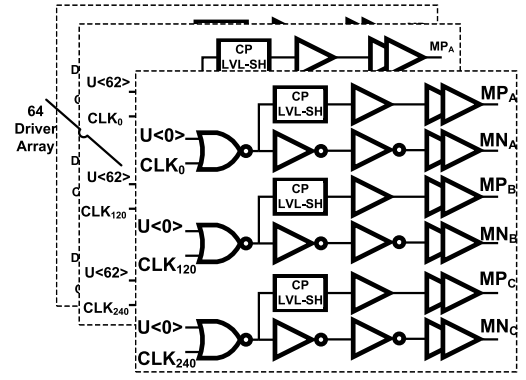
Fig. 11. Schematic of the bit-slice logic mixer, level shifter, and driver.
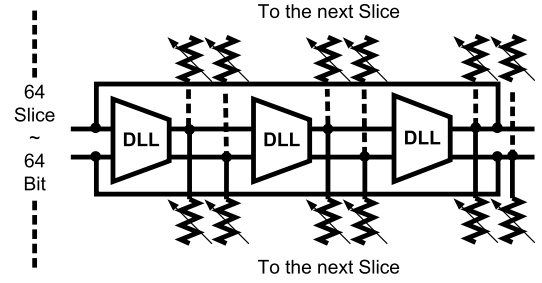
Fig. 12. Array of coupled DLLs.

For layout compactness, (13) can be used to find an Euler path. This allows the layout area to be reduced by minimizing the number of active diffusion breaks [31]. The abstract Euler path diagram for the pMOS and nMOS networks is shown in Fig. 10 (bottom). All devices within the nMOS and pMOS networks are matched following the Euler path. Hence, the edge-combining circuit is laid out in the most compact form, which is beneficial for the mmW operation. In addition, the location of $\text{MN}_{A/B/C}$ and $\text{MP}_{A/B/C}$ eases the layout of the input phase signals to better balance the resistive parasitics, which can further minimize the phase mismatch between $\Phi_{A/B/C}$ for both the pMOS and nMOS networks.

C. Bit-Slice Logical Mixer, Level Shifter, and Driver

It is important to drive the EC-SCPA output stage with square-wave signals that are appropriately phased aligned to maximize the efficiency. The driver slice operates at $f_{\text{out}}/3$ and powered from 0.9 V. Each bit slice has three branches supporting $\Phi_A = 0°$, $\Phi_B = 120°$, and $\Phi_C = 240°$, as shown in the schematic of Fig. 11. The tri-phase clocks are applied to their respective NOR gates that act as a logical mixer to mix the LO clock with the single unary bit input. This dictates whether the cell will either switch ON or be grounded. In the EC-SCPA output stage, the pMOS transistors operate between V_{DD} and $2V_{\text{DD}}$; therefore, level shifters are added to bring this path to the appropriate voltage domain. To reduce the power consumption, the dimensions of the devices in the NOR gate and level shifter are sized using logical effort scaling to optimize the power versus delay tradeoff. Delay must
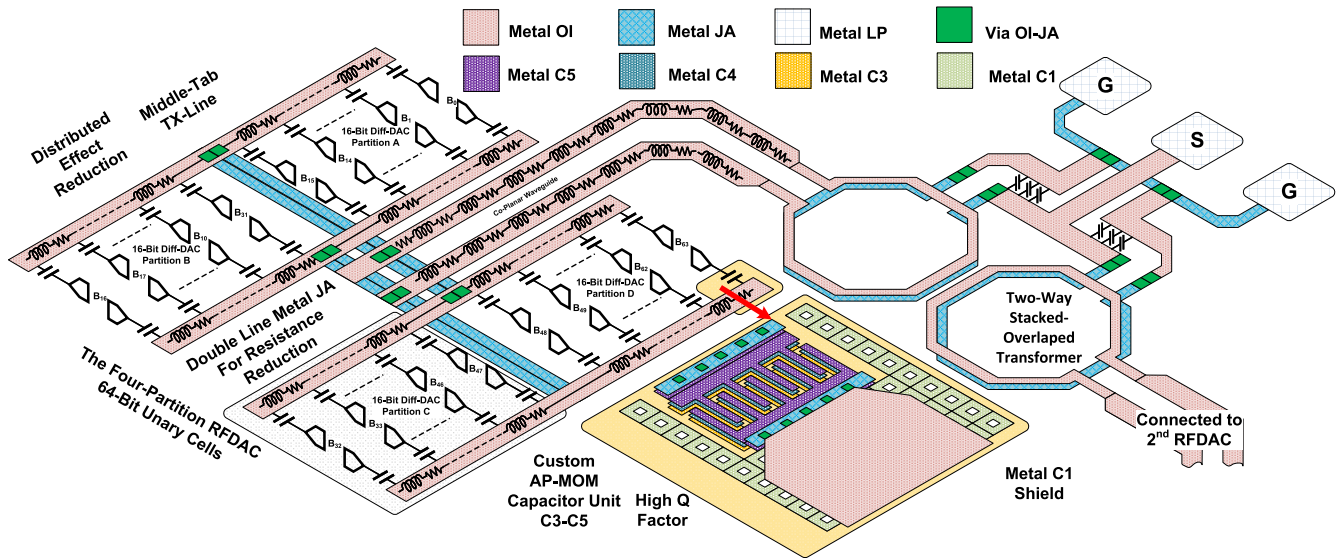
Fig. 13.   Implemented floorplan of the RFDAC core.

be carefully balanced in both the nMOS and pMOS paths. The buffered chains are carefully designed with post-layout extraction to ensure that all delay lines are correct to minimize the mismatch effect. This single bit slice is replicated into an array with 64 elements and drives on a bit-by-bit basis the 64 EC frequency-tripling switches.

D. Coupled DLL Network

The carrier clock must be evenly distributed to all 64 slices in the RFDAC core. At lower operational frequencies, this is typically accomplished with a standard H-tree. However, at mmW, this becomes extremely challenging as the carrier clock must arrive synchronously at each slice; also, the power consumption for the global clock distribution would increase. Our proposed solution is to generate carrier clocks locally in each slice via DLLs that are mutually coupled. The DLL is based on an RO as it provides the required phases and is fairly compact [32] to fit in the allotted place.

A standard differential three-delay-stage RO-based DLL is designed with injection locking based on the EC technique. As demonstrated in Section II, to further reduce the power dissipation without distributing the clock, the input reference of the DLL is chosen at $f_{out}/9$ with a 50% duty cycle in the range of 0–V_{DD}. The input is then applied to the EC stage before interpolating and generating $CLK_{0°}$, $CLK_{120°}$, and $CLK_{240°}$ at $f_{out}/3$. All of these circuits operate at $V_{DD} = 0.9$ V.

The mmW RFDAC requires 64 LO clock generators that can provide tri-phase $CLK_{0°}$, $CLK_{120°}$, and $CLK_{240°}$ from each generator, to drive the 64 RFDAC core unit cells. P_{out} will be degraded if the switching of any of the unit cells is not synchronous or has a poor edge slope. To overcome this challenge, a matrix of coupled DLLs is chosen, as shown in Fig. 12. Here, the coupling elements used for synchronization are resistors. The resistors value is chosen in the range of 20–80 Ω, which is calculated based on the Kuramoto model [33]. Because of the use of matrix coupling network,

the input injection signal must be strong enough to lock all 64 DLL units. In this way, all DLLs are synchronized via injection locking, which is explained by the Kuramoto model. Simulations validated that all tri-phase (e.g., $CLK_{0°}$, $CLK_{120°}$, and $CLK_{240°}$) signals are generated with sufficient accuracy to meet the output power, efficiency, and linearity requirements. The resulting phase errors will primarily reduce the output power and efficiency, as they will result in pulsewidth distortion and crow-bar currents. Secondarily, they can result in an impedance modulation of the switch, which can impact the linearity. The clock generation was validated across PVT to guarantee optimal output power and efficiency, which is also sufficient to guarantee linearity. In simulations across corners, a mismatch of <1 ps was observed across all rising and falling edges of the DLL outputs and the output duty cycle was maintained between 48.9% and 50.1%.

E. Separated Partition Layout

Floor planning plays an important role in RFDAC design, but at mmW becomes critical. Careful layout is necessary to ensure that the cells of the EC-SCPA operate in-phase and do not suffer degradation due to transmission-line (TL) effects. At lower frequency (e.g., sub-6 GHz), the wavelength is long relative to the size of the arrays in an RFDAC, but at mmW, this is not necessarily true. The distributed effects of the TLs can cause amplitude variation across the physical dimension of the array. For designs at this frequency, the lengths of the electrical connections at the same potential are explicitly shortened to be $L < \lambda/8$. In addition, the interconnect from the array to the PCT must be accounted for, as impedance variation due to the TL effects transforms Z_{opt}, which can reduce P_{out} and η_{SE} if not accounted for.

In sub-6-GHz SCPAs, the capacitor units were placed in the same direction in relatively large (dimensionally) arrays. This ensured the best linearity [2], [34]. However, applying this layout to mmW designs is not feasible due to the TL

effects on the top-plate connection of the capacitors, which would cause voltage variation across the plate. Each small section of TL is modeled with equivalent RLC, as shown in Fig. 13(b). It can be seen that TL effects can change the resonant frequency and impact the performance of the EC-SCPA. To solve this problem, the array is segmented into compact partitions, and the top plate is centrally connected. This minimizes the physical distance between capacitors, thus minimizing the parasitic inductances [35]. The 64-unary-bit array is divided into four partitions, each containing 16 cells. To connect the four partitions, a double TX line with a ground shield is designed to isolate the mmW TX line from the clock distribution network. A 3-D representation of the layout, where the output interconnect is shown in pink and the tapped interconnects are shown in blue, is shown in Fig. 13(b).

In addition to the interconnect, the quality (Q) factor of the unit capacitor is of concern. This is because the Q factor for capacitors at mmW can be degraded and thus impact the efficiency as in the case of inductors if care is not taken. The PDK p-cell capacitors are too dense and the layout results in a low component Q factor; hence, a custom AP-MoM unit capacitor is designed to obtain a high Q factor, as shown in the inset of Fig. 13. The custom MoM capacitor only uses metal C_1 as a shield while only using higher metal layers C_3, C_4, and C_5, to obtain the unit capacitance of 7.5 fF, while Q_C, which is simulated to be ≈ 58, is high enough to not degrade the matching network losses. Furthermore, to minimize the TL effects, the top-plate connection is designed in the highest metal layer with a taper.

IV. MEASUREMENT RESULTS

Prototype of the fully integrated Ka-Band SC-RFDAC was fabricated in a 22-nm FD-SOI process with 11 metal (including thick and ultra-thick) layers. The entire chip occupies 1.5×2 mm^2, including three pads for GSG RF probing, as shown in Fig. 14(a). To reduce noise coupling between the analog/RF and digital domains (high-speed data I/O and decoders), they are isolated via an undoped isolation ring (e.g., "BFMOAT" guard ring in our process PDK). Such an isolation ring has native doping of the bulk substrate, which is typically p^-. The RFDAC core draws high current but requires the power supply to be very stable; hence, eight supply pads are used, with the location well-distributed around the two RFDAC cores.

As shown in Fig. 13, each of the two RFDAC cores is split into four partitions. Each partition contains an array of 16-unary bit slices. All circuits besides the EC output stage operate at $V_{DD} = 0.9$ V, while the power supplies for the RFDAC output stage and drivers are set at $V_{DD2} = 1.8$ V. This is to account for the pMOS devices operating with the level shifting between V_{DD} and V_{DD2}.

A. Measurement Setup

The prototype chip is directly mounted on a PCB as "chip-on-board," in which all pads, except for the mmW output, are wirebonded. The entire assembly is placed on a Cascade M150 probe station, as shown in Fig. 14. The generated mmW output

(a)

(b)
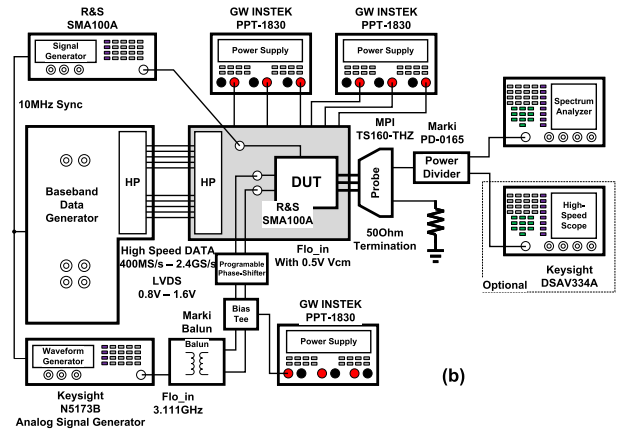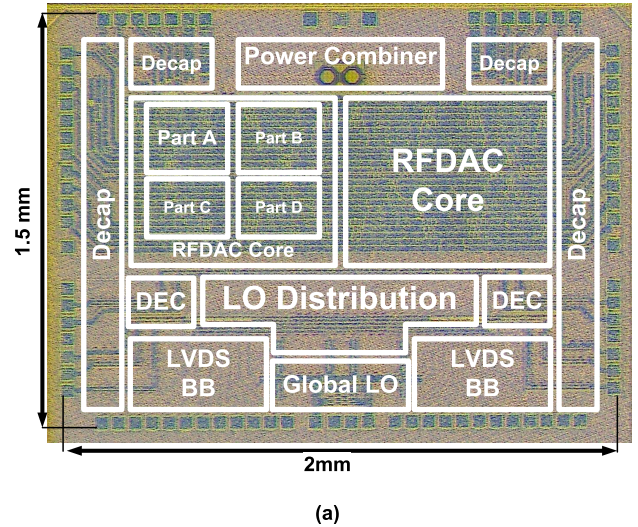
Fig. 14. (a) Chip microphotograph. Measurement setup: (b) diagram and (c) (d) photographs.

at the GSG pads is wafer-probed via MPI TITAN-T40A with a maximum insertion loss of -0.4 dB from 27 to 33 GHz. The probe output is then connected to a high-performance cable with a -1.4-dB loss before it is fed to the spectrum analyzer and the high-speed real-time oscilloscope for observation. The carrier clock input is provided by the Keysight N5173B Analog Signal Generator, which can support up to 20 GHz. The single-ended input is set between 2.5 and 3.5 GHz, with a default of 3.11 GHz. It is converted to differential one via the Marki Microwave Balun and passed through programmable phase shifters (not shown) and the bias tee to adjust its common-mode level. This helps to ensure proper injection locking of the on-chip oscillator. The baseband digital data are generated by the FPGA Ultrascale+ VCU, which is
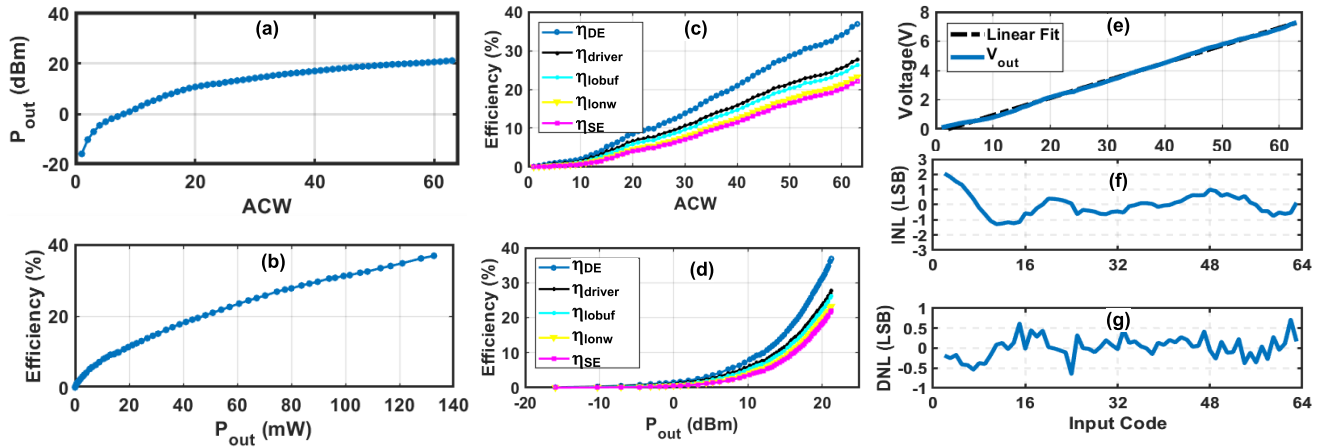
Fig. 15. Measured (a) P_{out} versus amplitude codeword (ACW). (b) Drain efficiency (η) versus P_{out}. (c) η, η_{SE}, and efficiencies in-between with various block contributions versus ACW. (d) Same data as in (c) but re-plotted versus P_{out}. (e) Measured RF output voltage versus ACW, resulting in (f) INL and (g) DNL nonlinearity.

Fig. 16. Measured modulation plots for 64-QAM at different bandwidths.

synchronized by a 10-MHz clock reference from SMA100A, feeding also the input LO for synchronization.

B. Static Measurements

The measured output power P_{out} at 27.9 GHz as a function of amplitude codeword (ACW), with the corresponding drain efficiency η as a function of P_{out}, is shown in Fig. 15(a) and (b). The peak P_{out} is 21.2 dBm at the maximum ACW. At the peak P_{out}, the drain efficiency $\eta = 36.7\%$, while at a 6-dB back-off, $\eta \approx 19\%$. The system efficiency, which incorporates power losses due to various blocks in the clock carrier distribution, is of paramount importance. The efficiency is broken down by the cumulative contributions and plotted as a function of ACW and P_{out} in Fig. 15(c) and (d), respectively,

to investigate the primary sources of degradation when compared to the drain efficiency, which only includes the output stage. The power consumption by the driver causes the primary degradation in η_{SE}, where the peak η_{driver} (clock buffering and clock generation are not yet included) is $\approx 27.6\%$. When including the remaining system blocks (e.g., clock buffering, digital logic, and clock generation), the total peak efficiency η_{SE} falls to 22%. It should be noted that this RFDAC is not just a PA but also provides the DAC and mixer functionality, thus comprising a full transmitter front end; hence, its η_{SE} is very competitive, even when compared to standalone PAs. The static level of RF output voltage versus ACW is plotted in Fig. 15(e). Its linearity can be quantified in terms of the integrated and differential nonlinearity (INL and DNL), as shown in Fig. 15(f) and (g). While delivering the peak

Carrier Frequency	28GHz	29GHz	30GHz
16-QAM Modulation			
64-QAM Modulation			
EVM-16QAM/64QAM	3.56% / 3.48%	3.84% / 3.77%	4.21% / 4.1%
Pk Avg Eff @ Data Rate	18.4% @ 2.4 Gb/s	16.2% @ 2.4 Gb/s	14.3% @ 2.4 Gb/s
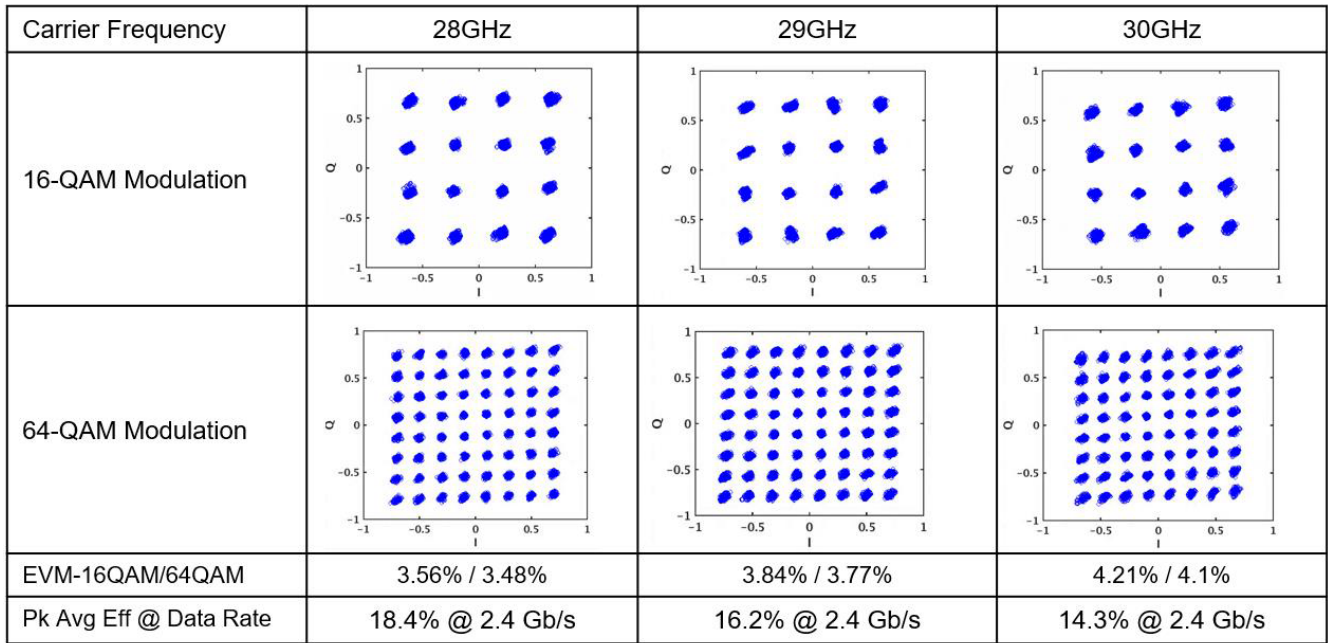
Fig. 17.   Measured modulation plots for 16-QAM and 64-QAM at different carrier frequencies.

TABLE I

PERFORMANCE SUMMARY AND COMPARISON WITH STATE OF THE ART FOR mmW TX/PA

	mmW DAC/Digital PA		mmW Outphasing			mmW Doherty		mmW Analog PA	
	This Work	Shopov JSSC'14	Kang JSSC'20	S. Li ISSCC'20	Li JSSC'19	Wang ISSCC'19	Hu ISSCC'17	Li ISSCC'18	Shakib ISSCC'17
Technology	**22nm CMOS SOI**	45nm CMOS SOI	45nm CMOS SOI	45nm CMOS SOI	45nm CMOS SOI	45nm CMOS SOI	130nm SiGe	130nm SiGe	40nm CMOS
Architecture	**Edge Combining Class D**	Stacked Current Mode	Current Mode Outphasing	Inverse Outphasing	Outphasing	Mixed-Signal Doherty	Multiband Doherty	Linear PA	Linear PA
DAC or PA	**RFDAC**	"Power DAC"	PA	Mixer + PA	Mixer + PA	PA	PA	PA	PA
Supply Voltage (V)	**0.9/1.8**	4.5-6	1.2	2	1	2	1.5	1.9	1.1
Resolution	**6-B**	6-B	N/A	N/A	N/A	N/A	N/A	N/A	N/A
Frequency (GHz)	**28**	32	30	29	28	27	28	28.5	27
Output Power (Peak) (dBm)	**21.2**	19.9	17	22.7	17.1	23.3	16.8	17	15.1
Efficiency @ Peak (%)	**36.7**	15.6	50.5*	42.6	43	40.1	20.3	43.5	33.7
Efficiency @ PBO (%)	**19**	N/A	40*	31	23	33	13.9	22	15.1
System Efficiency (%)	**22.1**	10.3	N/A	N/A	N/A	N/A	N/A	43.5	N/A
INL (LSB) DNL (LSB)	**< +2/-1 < +0.5/-0.5**	N/A	N/A	N/A	N/A	N/A	N/A	N/A	N/A
Data Rate (Gb/s)	**2.4**	12	3	15	6	15	6	18	4.8
Modulation	**64QAM**	64QAM	64QAM	64QAM	64QAM	64QAM	64QAM	64QAM	64QAM
EVM (dB)	**-29.6 (RMS)**	-28 (RMS)	-28 (RMS)	-22.5 (RMS)	-26.2 (RMS)	-24 (RMS)	-26.6 (Peak)	-25 (Peak)	-25 (RMS)
ACLR (dBc)	**-30.8**	N/A	N/A	-29.2	-28.3	N/A	-25.4	N/A	-29.4
DPD	**No**	No	LUT	LUT	LUT	No	No	No	No
Area (mm^2)	**2.2**	2.4	1.65	0.96	15	***0.52	1.76	***0.29	***0.225

* PA only   ** ACPR value   *** Core area only

output power of 21.2 dBm ($\sim$7 V_{pp}) at 27.9 GHz, the INL and DNL achieve excellent performance with $+2/-1$ LSB and $+0.5/-0.5$ LSB, chiefly due to the unit-weighted arrangement.

C. Dynamic Measurements

To validate the claimed potential of performance for modern wireless communication systems (e.g., 5G), several non-constant envelope-modulated signals are applied to evaluate the dynamic linearity.

The proposed RFDAC is measured using a 64-QAM signal across different modulation bandwidths (BW) at a center frequency of 27.9 GHz. The measured results are shown in Fig. 16. The EVM for BW = 100/200/400 MHz is, respectively, 3.15%/3.38%/3.32% rms. The respective average output power is 15.3/14.9/14.7 dBm, while the average system efficiency is 19.6%/18.8%/18.1%. All measurements are without any DPD applied. The performance remains stable up to BW = 400 MHz, which is limited by the output rate of the FPGA that acts as the pattern generator. The digital pattern is re-sampled on-chip to the input clock rate (i.e., $f_c/9$), which results in spectral images at this offset frequency from the f_c carrier. Though not implemented in this prototype, spectral images can be further mitigated using additional digital interpolation or analog linear interpolation [36].

The measured results for the 16-QAM (1.6 Gb/s) and 64-QAM (2.4 Gb/s) signals are shown from 28 to 30 GHz in Fig. 17. The output is tuned at 27.9 GHz and, hence, the performance is best at the center frequency. There is a slight rotation of the constellations resulting from the measurement instrument not fully nulling out the static phase offset. This is captured in the measured EVM. It is noted that the measured EVM and efficiency maintain good performance even when offset from the optimal tuning point. Although we were not able to increase the bandwidth beyond 400 MHz due to the limitations in our FPGA, we anticipate that memory effects caused by the supply network and output-matching network would limit the data rate. This is similar to the mechanisms that appear to malign all PAs. We note that, as with other PAs, these effects can typically be mitigated with a DPD.

V. Discussion and Conclusion

This article presents the first ever Ka-band switched-capacitor power-amplifier (SC-PA)-based RFDAC using an edge-combining technique. The proposed frequency tripler embedded in the output stage allows for the switching transistors to properly operate at mmW frequencies while maintaining good efficiency and linearity at >20-dBm output power. A comparison to prior art is shown in Table I. The work compares favorably to [19], which was an RF power-DAC operating at similar frequency and resolution. It also compares favorably to the mmW outphasing [17], [37], [38], mmW Doherty [39], [40], and linear mmW PAs [41], [42], noting that the proposed implementation delivers high output power while including the DAC+mixer functionality, whereas the other comparisons include fewer features. The presented approach is promising for other mmW hard-switching architectures as well, as frequency multiplication can be embedded into the output stages in Doherty and envelope elimination and restoration transmitters.

References

[1] P. Cruise et al., "A digital-to-RF-amplitude converter for GSM/GPRS/EDGE in 90-nm digital CMOS," in Proc. RFIC) Symp.,. Dig. Papers. IEEE Radio Freq. Integr. Circuits, Jun. 2005, pp. 21–24.

[2] S.-M. Yoo, J. S. Walling, E. C. Woo, B. Jann, and D. J. Allstot, "A switched-capacitor RF power amplifier," IEEE J. Solid State Circuits, vol. 46, no. 12, pp. 2977–2987, Dec. 2011.

[3] M. S. Alavi, R. B. Staszewski, L. C. N. D. Vreede, A. Visweswaran, and J. R. Long, "All-digital RF I/Q modulator," IEEE Trans. Microw. Theory Techn., vol. 60, no. 11, pp. 3513–3526, Nov. 2012.

[4] M. S. Alavi, R. B. Staszewski, L. C. N. de Vreede, and J. R. Long, "A wideband 2×13-bit all-digital I/Q RF-DAC," IEEE Trans. Microw. Theory Techn., vol. 62, no. 4, pp. 732–752, Apr. 2014.

[5] W. Yuan, V. Aparin, J. Dunworth, L. Seward, and J. S. Walling, "A quadrature switched capacitor power amplifier," IEEE J. Solid-State Circuits, vol. 51, no. 5, pp. 1200–1209, May 2016.

[6] V. Vorapipat, C. S. Levy, and P. M. Asbeck, "A class-G voltage-mode Doherty power amplifier," IEEE J. Solid-State Circuits, vol. 52, no. 12, pp. 3348–3360, Dec. 2017.

[7] B. Yang, E. Y. Chang, A. Niknejad, B. Nikolic, and E. Alon, "A 65nm CMOS I/Q RF power DAC with 24-42dB 3rd harmonic cancellation and up to 18dB mixed-signal filtering," in Proc. Symp. VLSI Circuits, Jun. 2017, pp. C302–C303.

[8] W. Yuan and J. S. Walling, "A multiphase switched capacitor power amplifier," IEEE J. Solid-State Circuits, vol. 52, no. 5, pp. 1320–1330, May 2017.

[9] Z. Bai, W. Yuan, A. Azam, and J. S. Walling, "4.3 A multiphase interpolating digital power amplifier for TX beamforming in 65nm CMOS," in IEEE ISSCC Dig. Tech. Papers, Feb. 2019, pp. 78–80.

[10] S.-W. Yoo, S.-C. Hung, J. S. Walling, D. J. Allstot, and S.-M. Yoo, "10.7 A 0.26 mm² DPD-less quadrature digital transmitter with 30dB pout range in 65nm CMOS," in IEEE ISSCC Dig. Tech. Papers, Feb. 2020, pp. 184–186.

[11] J. S. Walling, S. Yoo, and D. J. Allstot, "Multiphase switched-capacitor power amplifiers and bandpass digital transmitters," IEEE RFIC Virtual J., vol. 8, no. 12, pp. 1–12, Feb. 2016.

[12] Y. Yin et al., "A broadband switched-transformer digital power amplifier for deep back-off efficiency enhancement," IEEE J. Solid-State Circuits, vol. 55, no. 11, pp. 2997–3008, Nov. 2020.

[13] K.-S. Choi, J. Ko, and S.-G. Lee, "A single-supply single-core inverse class-D digital power amplifier with enhanced power back-off efficiency adopting output power scaling technique," in Proc. Symp. VLSI Circuits, Jun. 2021, pp. 1–2.

[14] H. J. Qian, B. Yang, J. Zhou, H. Xu, and X. Luo, "A quadrature digital power amplifier with hybrid Doherty and impedance boosting for complex domain power back-off efficiency enhancement," IEEE J. Solid-State Circuits, vol. 56, no. 5, pp. 1487–1501, May 2021.

[15] A. Zhang and M. S.-W. Chen, "A watt-level phase-interleaved multi-subharmonic switching digital power amplifier," IEEE J. Solid-State Circuits, vol. 54, no. 12, pp. 3452–3465, Dec. 2019.

[16] A. Zhang, C. Yang, M. Ayesh, and M. S.-W. Chen, "26.6 A 5-to-6GHz current-mode subharmonic switching digital power amplifier for enhancing power back-off efficiency," in IEEE ISSCC Dig. Tech. Papers, Feb. 2021, pp. 364–366.

[17] S. Li, M.-Y. Huang, D. Jung, T.-Y. Huang, and H. Wang, "24.3 A 28GHz current-mode inverse-outphasing transmitter achieving 40%/31% PA efficiency at Psat/6dB PBO and supporting 15Gbit/s 64-QAM for 5G communication," in IEEE ISSCC Dig. Tech. Papers, Feb. 2020, pp. 366–368.

[18] F. Wang and H. Wang, "24.1 A 24-to-30GHz watt-level broadband linear Doherty power amplifier with multi-primary distributed-active-transformer power-combining supporting 5G NR FR2 64-QAM with >19dBm average pout and >19% average PAE," in *IEEE ISSCC Dig. Tech. Papers*, Feb. 2020, pp. 362–364.

[19] S. Shopov, A. Balteanu, and S. P. Voinigescu, "A 19 dBm, 15 Gbaud, 9 bit SOI CMOS power-DAC cell for high-order QAM W-band transmitters," *IEEE J. Solid-State Circuits*, vol. 49, no. 7, pp. 1653–1664, Jul. 2014.

[20] S. Shopov, N. Cahoon, and S. P. Voinigescu, "Ultra-broadband I/Q RF-DAC transmitters," *IEEE Trans. Microw. Theory Techn.*, vol. 65, no. 12, pp. 5411–5421, Dec. 2017.

[21] K. Dasgupta, S. Daneshgar, C. Thakkar, K. Datta, J. Jaussi, and B. Casper, "A 25 Gb/s 60 GHz digital power amplifier in 28nm CMOS," in *Proc. 43rd IEEE Eur. Solid State Circuits Conf. (ESSCIRC)*, Sep. 2017, pp. 207–210.

[22] K. Khalaf et al., "Digitally modulated CMOS polar transmitters for highly-efficient mm-wave wireless communication," *IEEE J. Solid-State Circuits*, vol. 51, no. 7, pp. 1579–1592, Jul. 2016.

[23] M. Babaie, R. B. Staszewski, L. Galatro, and M. Spirito, "A wideband 60 GHz class-E/F$_2$ power amplifier in 40nm CMOS," in *Proc. IEEE Radio Freq. Integr. Circuits Symp. (RFIC)*, May 2015, pp. 215–218.

[24] P. Madoglio et al., "A 20dBm 2.4GHz digital outphasing transmitter for WLAN application in 32nm CMOS," in *Proc. IEEE Int. Solid-State Circuits Conf.*, Feb. 2012, pp. 168–170.

[25] M. Fulde et al., "13.2 A digital multimode polar transmitter supporting 40MHz LTE carrier aggregation in 28nm CMOS," in *IEEE ISSCC Dig. Tech. Papers*, Feb. 2017, pp. 218–219.

[26] P. Madoglio et al., "13.6 A 2.4GHz WLAN digital polar transmitter with synthesized digital-to-time converter in 14nm trigate/FinFET technology for IoT and wearable applications," in *IEEE ISSCC Dig. Tech. Papers*, Feb. 2017, pp. 226–227.

[27] P. Madoglio et al., "A cellular multiband DTC-based digital polar transmitter with –153-dBc/Hz noise in 14-nm FinFET," *IEEE J. Solid-State Circuits*, vol. 55, no. 7, pp. 1830–1841, Jul. 2020.

[28] Q. J. Gu, Z. Xu, and M.-C. F. Chang, "Two-way current-combining W-band power amplifier in 65-nm CMOS," *IEEE Trans. Microw. Theory Techn.*, vol. 60, no. 5, pp. 1365–1374, Mar. 2012.

[29] H. Ahn, K. Oh, I. Nam, and O. Lee, "A highly efficient and linear mm-wave CMOS power amplifier using a compact symmetrical parallel–parallel power combiner with IMD3 cancellation for 5G applications," *IEEE Access*, vol. 9, pp. 150304–150321, 2021.

[30] A. Azam, Z. Bai, and J. S. Walling, "Leveraging programmable capacitor arrays for frequency-tunable digital power amplifiers," *IEEE Trans. Microw. Theory Techn.*, vol. 68, no. 6, pp. 1983–1994, Jun. 2020.

[31] A. C. Jan, M. Rabaey, and B. Nikolic, *Digital Integrated Circuits*, 2nd ed. London, U.K.: Pearson, 2002.

[32] S. L. J. Gierkink, "Low-spur, low-phase-noise clock multiplier based on a combination of PLL and recirculating DLL with dual-pulse ring oscillator and self-correcting charge pump," *IEEE J. Solid-State Circuits*, vol. 43, no. 12, pp. 2967–2976, Dec. 2008.

[33] N. Chopra and M. W. Spong, "On synchronization of Kuramoto oscillators," in *Proc. 44th IEEE Conf. Decis. Control*, Dec. 2005, pp. 3916–3922.

[34] Z. Bai, A. Azam, D. Johnson, W. Yuan, and J. S. Walling, "Split-array, C-2C switched-capacitor power amplifiers," *IEEE J. Solid-State Circuits*, vol. 53, no. 6, pp. 1666–1677, Jun. 2018.

[35] J. S. Walling et al., "A class-E PA with pulse-width and pulse-position modulation in 65 nm CMOS," *IEEE J. Solid-State Circuits*, vol. 44, no. 6, pp. 1668–1678, Jun. 2009.

[36] F. Zhang, P. Chen, J. S. Walling, A. Zhu, and R. B. Staszewski, "An active-under-coil RFDAC with analog linear interpolation in 28-nm CMOS," *IEEE Trans. Circuits Syst. I, Reg. Papers*, vol. 68, no. 5, pp. 1855–1868, May 2021.

[37] K. Ning, Y. Fang, N. Hosseinzadeh, and J. F. Buckwalter, "A 30-GHz CMOS SOI outphasing power amplifier with current mode combining for high backoff efficiency and constant envelope operation," *IEEE J. Solid-State Circuits*, vol. 55, no. 5, pp. 1411–1421, May 2020.

[38] S. Li, T. Chi, J.-S. Park, H. T. Nguyen, and H. Wang, "A 28-GHz flip-chip packaged Chireix transmitter with on-antenna outphasing active load modulation," *IEEE J. Solid-State Circuits*, vol. 54, no. 5, pp. 1243–1253, May 2019.

[39] F. Wang, T.-W. Li, and H. Wang, "4.8 A highly linear super-resolution mixed-signal Doherty power amplifier for high-efficiency mm-wave 5G multi-Gb/s communications," in *IEEE ISSCC Dig. Tech. Papers*, Feb. 2019, pp. 88–90.

[40] S. Hu, F. Wang, and H. Wang, "2.1 A 28GHz/37GHz/39GHz multiband linear Doherty power amplifier for 5G massive MIMO applications," in *IEEE ISSCC Dig. Tech. Papers*, Feb. 2017, pp. 32–33.

[41] T.-W. Li, M.-Y. Huang, and H. Wang, "A continuous-mode harmonically tuned 19-to-29.5GHz ultra-linear PA supporting 18Gb/s at 18.4% modulation PAE and 43.5% peak PAE," in *IEEE ISSCC Dig. Tech. Papers*, Feb. 2018, pp. 410–412.

[42] S. Shakib, M. Elkholy, J. Dunworth, V. Aparin, and K. Entesari, "2.7 A wideband 28GHz power amplifier supporting 8×100MHz carrier aggregation for 5G in 40nm CMOS," in *IEEE ISSCC Dig. Tech. Papers*, Feb. 2017, pp. 44–45.

Hieu Minh Nguyen (Graduate Student Member, IEEE) received the B.E. and M.E. degrees in electronics and telecommunication engineering from the Ho Chi Minh City University of Technology, Ho Chi Minh City, Vietnam, in 2014 and 2016, respectively. He is currently pursuing the Ph.D. degree with the IoE Laboratory, University College Dublin, Dublin, Ireland.

From 2013 to 2014, he joined the Integrated Circuit Design Research and Education Center, where he studied analog and RF integrated circuit design. From 2014 to 2015, he worked as a Teaching and Research Assistant with the Department of Electronics Engineering, Faculty of Electrical and Electronics Engineering, Ho Chi Minh City University of Technology. From 2015 to 2017, he worked as an Analog IC Design Engineer with Uniquify, San Jose, CA, USA, where he focused on the PHY and SERDES systems. His research interests include digital power amplifiers, RFDACs, and RF integrated circuit design.

Mr. Nguyen is also serving as a Reviewer for IEEE JOURNAL OF SOLID-STATE CIRCUITS (JSSC), IEEE TRANSACTIONS ON CIRCUITS AND SYSTEMS I: REGULAR PAPERS (TCAS I) and IEEE TRANSACTIONS ON CIRCUITS AND SYSTEMS II: EXPRESS BRIEFS (TCAS II), and IEEE TRANSACTIONS ON MICROWAVE THEORY AND TECHNIQUES (TMTT). He received the Award of Best Student in Analog IC Design for the Design of 24-bit Delta-Sigma ADC.

Jeffrey Sean Walling (Senior Member, IEEE) received the B.S. degree from the University of South Florida, Tampa, FL, USA, in 2000, and the M.S. and Ph.D. degrees from the University of Washington, Seattle, WA, USA, in 2005 and 2008, respectively.

Prior to starting his graduate education, he was employed with Motorola Solutions, Plantation, FL, USA, working in cellular handset development. He interned for Intel, Hillsboro, OR, USA, from 2006 to 2007. He was a Post-Doctoral Research Associate with the University of Washington from 2008 to 2010. He was an Assistant Professor with the Department of Electrical and Computer Engineering (ECE), Rutgers University, New Brunswick, NJ, USA, from 2011 to 2012, and then an Assistant Professor and later an Associate Professor with the Department of ECE, The University of Utah, Salt Lake, UT, USA, from 2012 to 2018. He was the Head of Group (RF Transceivers) in the Microelectronic Circuits Centre Ireland, Tyndall National Institute, Cork, Ireland, in 2019. He is currently an Associate Professor with Virginia Tech, Blacksburg, VA, USA. He has authored more than 70 papers in peer-reviewed journals and refereed conferences. His research interests include high-efficiency digital transmitter architectures and power amplifier design.

Dr. Walling received the Analog Devices Outstanding Student Designer Award in 2006, an Intel Predoctoral Fellowship from 2007 to 2008, the Yang Award for Outstanding Graduate Research from the Department of Electrical Engineering (EE), University of Washington, in 2008, the Best Paper Award from MobiCom in 2012, the Excellence in Teaching Award from HKN, Rutgers University, in 2012, and the Award for Outstanding Teaching from The University of Utah in 2015.

Anding Zhu (Fellow, IEEE) received the Ph.D. degree in electronic engineering from the University College Dublin (UCD), Dublin, Ireland, in 2004.

He is currently a Professor with the School of Electrical and Electronic Engineering, UCD. His research interests include high-frequency nonlinear system modeling and device characterization techniques, high-efficiency power amplifier design, wireless transmitter architectures, digital signal processing, and nonlinear system identification algorithms.

Prof. Zhu has served as the Secretary for the IEEE Microwave Theory and Techniques Society (MTT-S) Administrative Committee (AdCom) in 2018. He is also an Elected Member of MTT-S AdCom, the Chair of the Electronic Information Committee, and the Vice Chair of the Marketing and Communications Committee. He was the General Chair of the 2018 IEEE MTT-S International Microwave Workshop Series on 5G Hardware and System Technologies (IMWS-5G) and the Guest Editor of the IEEE TRANSACTIONS ON MICROWAVE THEORY AND TECHNIQUES on 5G Hardware and System Technologies. He is also a Track Editor of the IEEE TRANSACTIONS ON MICROWAVE THEORY AND TECHNIQUES and an Associate Editor of *IEEE Microwave Magazine*.

Robert Bogdan Staszewski (Fellow, IEEE) was born in Bialystok, Poland. He received the B.Sc. *(summa cum laude)*, M.Sc., and Ph.D. degrees in electrical engineering from The University of Texas at Dallas, Richardson, TX, USA, in 1991, 1992, and 2002, respectively.

From 1991 to 1995, he was with Alcatel Network Systems, Richardson, involved in SONET cross-connect systems for fiber optics communications. He joined Texas Instruments Inc., Dallas, TX, USA, in 1995, where he was elected as a Distinguished Member of Technical Staff (limited to 2% of technical staff). From 1995 to 1999, he was involved in advanced CMOS read channel development for hard disk drives. In 1999, he co-started the Digital RF Processor (DRP) Group, Texas Instruments, with a mission to invent new digitally intensive approaches to traditional RF functions for integrated radios in deeply scaled CMOS technology. He was appointed as the CTO of the DRP group from 2007 to 2009. In 2009, he joined the Delft University of Technology, Delft, The Netherlands, where he currently holds a guest appointment of Full Professor *(Antoni van Leeuwenhoek Hoogleraar)*. Since 2014, he has been a Full Professor with the University College Dublin (UCD), Dublin, Ireland. He is also a Co-Founder of a startup company, Equal1 Labs, with design centers located in Silicon Valley and Dublin, Ireland, aiming to produce single-chip CMOS quantum computers. He has authored or coauthored six books, 11 book chapters, and 150 journal and 210 conference publications. He holds 210 issued U.S. patents. His research interests include nanoscale CMOS architectures and circuits for frequency synthesizers, transmitters and receivers, and quantum computers.

Prof. Staszewski was a recipient of the 2012 IEEE Circuits and Systems Industrial Pioneer Award. He is on the Technical Program Committee of the VLSI Symposium on Circuits.